# Melt network reorientation and crystallographic preferred orientation development in sheared partially molten rocks

Cassandra Seltzer[1], Matěj Peč[2], Mark E. Zimmerman[3], and David L Kohlstedt[3]

[1]Massachusetts Institute of Technology
[2]MIT EAPS
[3]University of Minnesota

September 11, 2023

## Abstract

As partially molten rocks deform, they develop melt preferred orientations, shape preferred orientations, and crystallographic preferred orientations (MPOs, SPOs and CPOs). We investigated the co-evolution of these preferred orientations in experimentally deformed partially molten rocks, then calculated the influence of MPO and CPO on seismic anisotropy. Olivine-basalt aggregates containing 2 to 4 wt% melt were deformed in general shear at a temperature of 1250°C under a confining pressure of 300 MPa at shear stresses of $\tau = 0$ to 175 MPa to shear strains of $\gamma = 0$ to 2.3. Grain-scale melt pockets developed a MPO parallel to the maximum principal stress, s1, at $\gamma < 0.4$. At higher strains, the grain-scale MPO remained parallel to s1, but incipient, sample-scale melt bands formed at ˜20° to s1. An initial SPO and CPO were induced during sample preparation, with [100] and [001] axes girdled perpendicular to the long axis of the sample. At the highest explored strain, a strong SPO was established, and the [100] axes of the CPO clustered nearly parallel to the shear plane. Our results demonstrate that grain-scale and sample-scale alignments of melt pockets are distinct. Furthermore, the melt and the solid microstructures evolve on different timescales: in planetary bodies, changes in the stress field will first drive a relatively rapid reorientation of the melt network, followed by a relatively slow realignment of the crystallographic axes. Rapid changes to seismic anisotropy in a deforming partially molten aggregate are thus caused by MPO rather than CPO.

## Hosted file

`957019_0_art_file_10738493_rqjvn7.docx` available at https://authorea.com/users/589742/articles/626431-melt-network-reorientation-and-crystallographic-preferred-orientation-development-in-sheared-partially-molten-rocks

# Melt network reorientation and crystallographic preferred orientation development in sheared partially molten rocks

C. Seltzer[1], M. Peč[1], M.E. Zimmerman[2], D.L. Kohlstedt[2]

[1]Department of Earth, Atmospheric and Planetary Sciences, Massachusetts Institute of Technology, Cambridge, MA 02139

[2]Department of Earth and Environmental Sciences, University of Minnesota, Minneapolis, MN 55455

Corresponding author: Cassandra Seltzer (cseltz@mit.edu)

## Key Points

1. When a partially molten rock is stressed, its microstructural melt pockets reorient much more quickly than its crystallographic axes.
2. Individual melt pockets orient parallel to the loading direction at the onset of deformation.
3. Rapid changes to seismic anisotropy in a deforming partially molten rock can be attributed to reorientation of melt pockets.

**Abstract**:

We investigated the co-evolution of melt, shape, and crystallographic preferred orientations (MPOs, SPOs and CPOs) in experimentally deformed partially molten rocks, from which we calculated the influence of MPO and CPO on seismic anisotropy. Olivine-basalt aggregates containing 2 to 4 wt% melt were deformed in general shear at a temperature of 1250°C under a confining pressure of 300 MPa at shear stresses of $\tau \leq 175$ MPa to shear strains of $\gamma \leq 2.3$. Grain-scale melt pockets developed a MPO parallel to the loading direction by $\gamma < 0.4$. At higher strains, the grain-scale MPO remained parallel to the loading direction, while incipient, sample-scale melt bands formed at ~20° to the grain-scale MPO. An initial SPO and CPO were induced during sample preparation, with [100] and [001] axes girdled perpendicular to the long axis of the starting material. At the highest explored strain, a strong SPO was established subperpendicular to the loading direction, and the [100] axes of the CPO clustered nearly parallel to the shear plane. Our results demonstrate that grain-scale and sample-scale alignments of melt pockets are distinct. Furthermore, the melt and the solid microstructures evolve on different timescales: in planetary bodies, changes in the stress field will drive a relatively rapid reorientation of the melt network and a relatively slow realignment of the crystallographic axes. Rapid changes to seismic anisotropy in a deforming partially molten aggregate are thus caused by MPO rather than CPO.

Plain language summary:

We studied the influence of melt alignment and crystal alignment on the properties of partially melted regions in planetary bodies. Molten and crystalline elements within the rocks in these layers can deform and reorient in response to stress, but it is difficult to predict how the effect of realignment of each phase affects seismic properties of the rocks. Reorientation of melt networks during deformation of partially molten rocks is not well constrained, as experiments and computational models disagree on the most favorable alignment of melt pockets. Here, we measured the angles and shapes of melt and crystals in experimentally deformed partially molten rocks, then calculated seismic properties of the deformed rocks. We found that melt pockets change orientation and shape quickly, but crystallographic axes take longer to reorient. This observation indicates that immediate changes to seismic properties after a sudden change in stress field are caused by melt, rather than by crystals. Our results show that when stress fields abruptly change in Earth and other planetary bodies, melt pocket orientation controls seismic properties and is the best instantaneous indicator of stress changes.

## 1. Introduction

Partial melting often occurs alongside sites of rapid deformation in Earth's lithosphere. In response to deformation, the molten and crystalline components of partially molten rocks align, leading to anisotropies in mechanical, transport, and seismic properties (Blackman & Kendall, 1997; Daines & Kohlstedt, 1997; Holtzman et al., 2003; Holtzman & Kendall, 2010; Long & Becker, 2010; Savage, 1999; Taylor-West & Katz, 2015). The influence of microstructure on seismic properties, in particular, is often considered only in terms of the crystalline components, but this approach may not be sufficient for interpreting the effects of deformation in partially molten regions. Melt is known to change the physical properties of an aggregate even in small concentrations, as the molten and solid rock components have distinct seismic properties. The orientations of both phases therefore contribute to the seismic anisotropy observed in Earth's upper mantle and crust (Almqvist & Mainprice, 2017; Hansen et al., 2021; Lyakhovsky et al., 2021). Laboratory experiments provide an important tool for determining melt and crystallographic preferred orientations in deformed partially molten mantle rocks. However, experimental results and modeling assumptions often disagree on the orientation of the melt network. Previous experimental studies reported alignment of the long axes of melt pockets at 20° to the direction of the inferred maximum principal stress (Zimmerman et al., 1999, Soustelle et al., 2014, Danies and Kohlstedt, 1997) and, with increasing strain, the formation of melt-rich "bands" at a similar orientation (Holtzman et al., 2003; King et al., 2010; see Kohlstedt & Holtzman, 2009 and Daines & Pec, 2015 for comprehensive reviews of observed melt alignment in experiments). In contrast, some viscoelastic models and theories assume grain-scale melt alignment parallel to the direction of the maximum principal stress, $\sigma_1$ (Hier-Majumder, 2011; Takei & Holtzman, 2009c; Taylor-West & Katz, 2015), an orientation of melt alignment which has also been reported using ultrasonic measurements in experiments on analog materials (Takei, 2001). To resolve differences between modeling, nature, and experimental results, we reexamined microstructures of deformed partially molten samples.

The present study investigates the microstructural behavior of several partially molten olivine + basalt aggregates deformed in general shear experiments. The sample-scale behavior of one set of samples was previously reported in Zimmerman et al. (1999). In addition, the behavior of two additional samples deformed at higher stress conditions was examined. We characterize the co-evolution of melt preferred orientation (MPO) of the liquid network and crystallographic and shape preferred orientations (CPOs and SPOs) of the solid phase, from which we infer the influence of stress and strain on CPO, SPO and MPO development in the deformed samples. We then use our experimental results to calculate predicted seismic anisotropy in these samples. Finally, we discuss the relative importance of the orientations of melt pockets and crystallographic axes on seismic anisotropy in samples deformed to small strains.

## 2. Methods

### *2.1 Experimental deformation and imaging details*

Samples of olivine ± orthopyroxene and 2-4 wt% mid-ocean ridge basalt (MORB) were created by hot pressing cold-pressed powders in a gas-medium deformation apparatus (Paterson, 1990) at 1250ºC at 300 MPa for ~3 h. At these temperature and pressure conditions, MORB inclusions melted, while solid olivine crystals did not, thus forming a dense, chemically equilibrated partially molten aggregate (Cooper & Kohlstedt, 1984). Samples were then cored and sliced from the hot-pressed cylinders and placed between thoriated-tungsten pistons pre-cut at a 45º angle, as illustrated in Figure 1. These samples were subsequently deformed in general shear at the University of Minnesota in the gas-medium deformation apparatus at 1250ºC and 300 MPa confining pressure. Under strain rates of $10^{-6}$-$10^{-4}$ $s^{-1}$, samples reached shear stresses of $\tau$ = 50-175 MPa and strains of $\gamma$ = 0.32-2.3. A summary of the experimental conditions and resultant MPO and SPOs presented in Table 1.

| # | T (°C) | $\gamma_{meas}$ | $\gamma'$ ($s^{-1}$) | $\sigma_{effective}$ (MPa) | $\tau_{final}$ (MPa) | initial thickness (mm) | final thickness (mm) | MPO $\alpha_p$ (°) | MPO *b/a* | SPO $\alpha_p$ (°) | SPO *b/a* | $W_k$ |
|---|---|---|---|---|---|---|---|---|---|---|---|---|
| starting material | 1250 | - | - | - | - | - | - | 160 | 0.97 | 20 | 0.88 | - |
| PI-281 | 1250 | 0.32 | $1.7 \times 10^{-6}$ | 110 | 55 | 0.65 | 0.61 | 135 | 0.8 | 13 | 0.94 | - |
| PI-277 | 1250 | 0.4 | $6.5 \times 10^{-5}$ | 132 | 66 | 0.82 | 0.8 | 134 | 0.72 | 11 | 0.89 | 0.99 |
| PI-334 | 1250-1290 | 0.77 | * | 350 | 175 | 0.8 | 0.66 | 112 | 0.74 | 30 | 0.89 | 0.97 |
| PI-314 | 1250 | 0.84 | $4 \times 10^{-5}$ | 300 | 150 | 0.81 | 0.71 | 130 | 0.82 | 31 | 0.93 | 0.92 |
| PI-274 | 1250 | 1.3 | $2.7 \times 10^{-5}$ | 100 | 50 | 0.83 | 0.72 | 132 | 0.77 | 32 | 0.79 | 0.96 |
| PI-273 | 1250 | 2.3 | $4.0 \times 10^{-4}$ | 180 | 90 | 0.93 | 0.76 | 134 | 0.77 | 26 | 0.73 | 0.98 |

Table 1: Experimental parameters for starting material and six deformed samples. Here, $\gamma$ indicates strain, $\tau_{final}$ is the inferred shear stress, and $W_k$ denotes the kinematic vorticity number, expressing the ratio of simple shear to pure shear (see Section 4.2). The initial thickness of PI-281 was measured, but not its initial width, so its kinematic vorticity could not be calculated.

After deformation, samples were cut perpendicular to the shear plane and parallel to the shear direction, as indicated in Figure 2. A Zeiss Merlin scanning electron microscope (SEM) in the MIT Materials Research Laboratory was used to create backscattered electron (BSE) images at 15 – 20 kV accelerating voltage of these 2-D flat sections. In addition, electron backscattered diffraction (EBSD) maps and energy dispersive spectra (EDS) maps were collected using a Camscan X500FE CrystalProbe at the Université Montpellier 2 at an acceleration voltage of 20 kV and a step size of 0.2 – 0.6 µm.

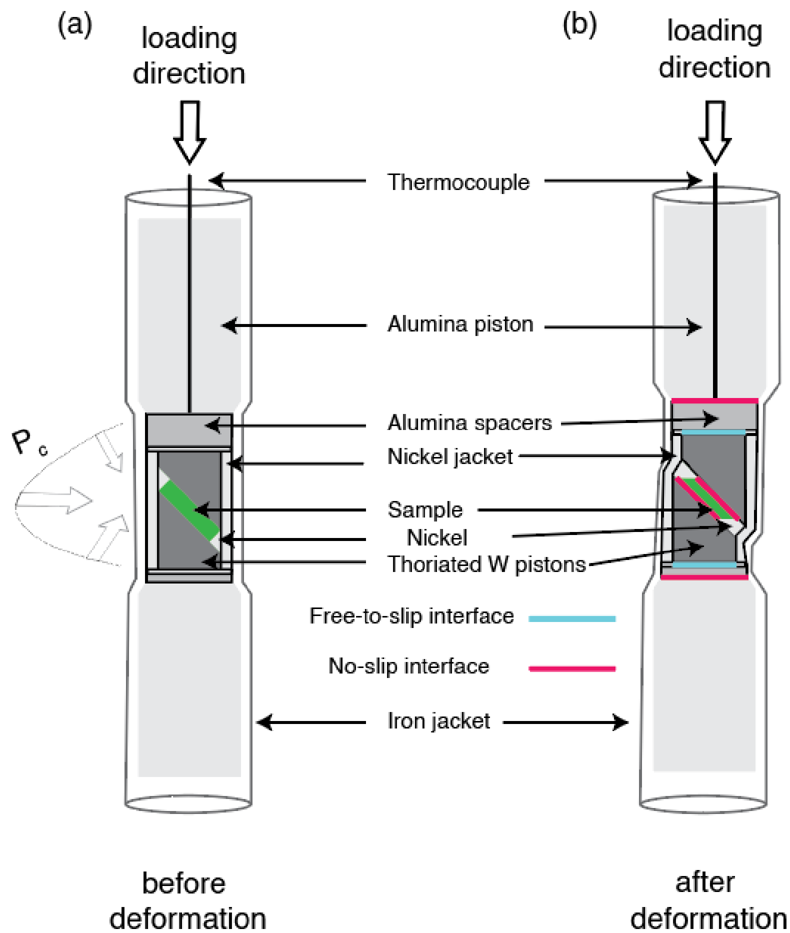


Figure 1: Schematic drawing of the sample setup for deformation experiments.

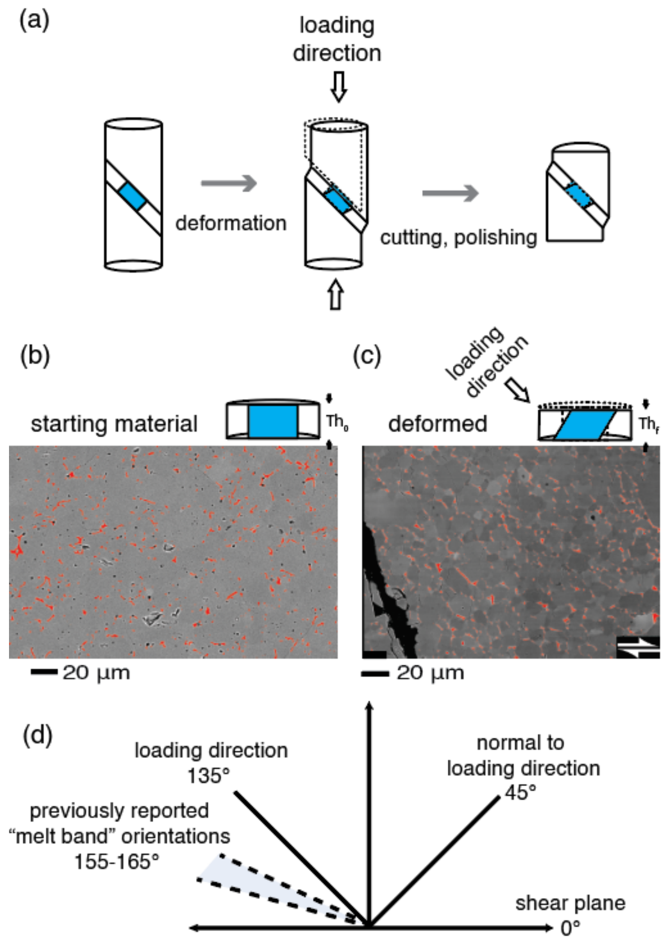


Figure 2: Sample preparation after deformation and orientation of cuts. (a) Experimental workflow for deformation and creation of 2-D sections. SEM images of orientation and appearance of the olivine-melt aggregates (b) prior to deformation, at initial thickness $Th_0$, and (c) after deformation, at final thickness $Th_f$, with melt highlighted in red. (d) Angle conventions used throughout this paper.

## 2.2 *Quantitative image analysis methods*

We used the PARticle ORientation method (PAROR; Heilbronner and Barrett, 2014, Chapter 14) to analyze the grain-scale MPOs and SPOs. This method yields the direction of the longest and shortest projections of particle elements. In contrast to the more common ellipse-fitting method of determining orientation of short and long axes, PAROR does not require the shortest and longest projection directions to be perpendicular to each other and is therefore well suited for analyzing shapes of irregular objects such as melt pockets. Any shape with long axis *a* and short axis *b* is characterized by a projection function at a range of angles α, such that

$$P(\alpha) = 2\sqrt{a^2\cos^2(\alpha_i + \alpha_r) + b^2\sin^2(\alpha_i + \alpha_r)} \quad , \qquad (1)$$

where α is constructed by starting at an initial orientation $\alpha_i$ and incremented by $\alpha_r$ over a range of angles. This projection is symmetric around 180˚. *P*(α) will be largest at the same orientation as *a*, and smallest at the orientation of *b*. For aggregates of shapes, the distribution function at each value of α is characterized by the sum of the values of *P*(α), then scaled such that $\Sigma P(\alpha)_{\max} = 1$.

The preferred orientation angle, $\alpha_p$, is then calculated relative to the shortest projection direction $\alpha_{min}$ such that

$$\alpha_p = 90^\circ - \alpha_{\min} \, . \qquad (2)$$

As values of $\alpha_p$ are symmetric around 180˚, for $\alpha_{min} > 90$˚, negative values are converted to their positive conjugate (i.e., -30˚ is the same as 150˚). Angles are measured counterclockwise from 0° (east) to 180° (west) throughout this manuscript, as illustrated in Figure 2d.

We described the orientations of grains and melt pockets using an orientation distribution function (ODF) visualized as rose diagrams, normalized such that the longest axis is 1 and the shortest axis is reported as a percentage relative to the longest axis, as illustrated in Figure 3.

The strength of the preferred orientation is quantified by its bulk aspect ratio, *b*/*a*, a comparison of the longest, *a*, and the shortest, *b*, projections of all the analyzed melt pockets. The ratio is defined from 0 to 1, such that a *b*/*a* ratio close to 1 indicates that little difference exists between the shortest and longest axes and that the shape is close to isotropic. In contrast, a smaller value of *b*/*a* indicates a stronger preferred orientation. We also calculated the size of segmented objects as an equivalent area circle with diameter $d_{equ}$. Because both melt pocket size and grain size distributions frequently follow a log-normal distribution, we report the mode of the log-normal probability distribution as the most common size for melt pockets or grains in each sample.

We analyzed the orientation of a sample-scale melt network with the autocorrelation function (ACF; Heilbronner and Barrett, 2014, Chapter 20). The autocorrelation function quantifies the orientation and spatial frequency of the patterns in an image without the segmentation of individual features. For a given feature defined by the gray value function G(x,y) at coordinates (x, y), reoccurring at a displacement (x', y'), the ACF is defined as the convolution of G(x,y) with itself such that

$$G(x,y) * G(x,y) = \int_{-\infty}^{\infty}\int_{-\infty}^{\infty} G(x',y') \cdot G(x+x',y+y')\, dx'dy' \quad . \qquad (3)$$

The output of the ACF shows the orientation of features, as well as the length scale over which they repeat themselves. This approach is therefore well suited for analyzing large-scale, fine-feature patterns.

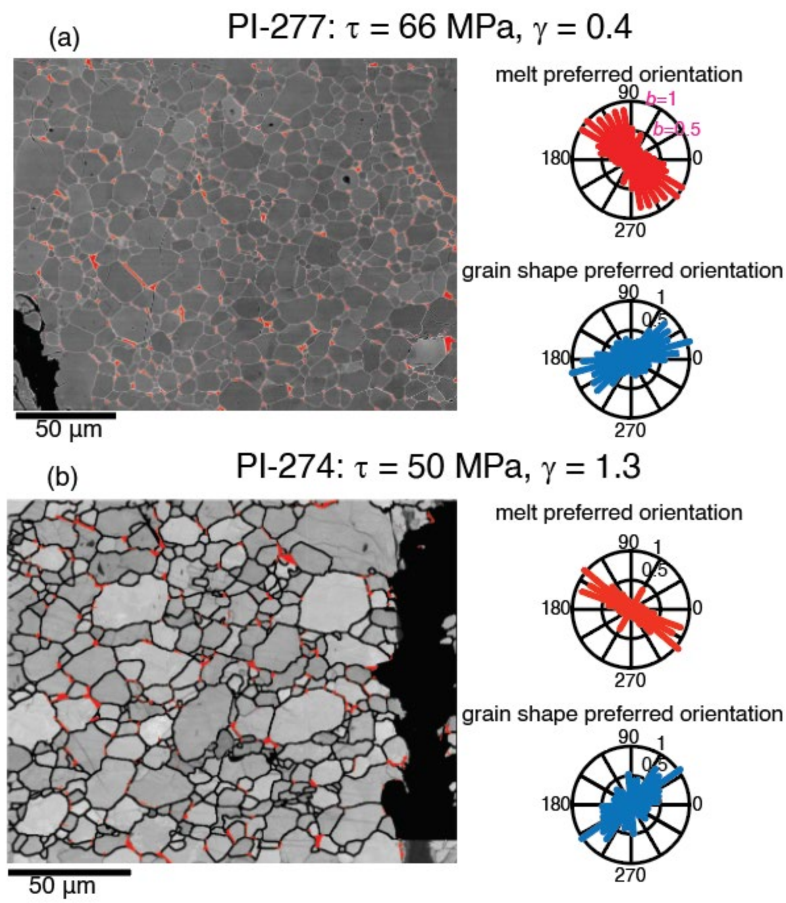


Figure 3: 2-D maps of two samples, one deformed to (a) low strain and the other to (b) high strain. The grains are outlined in black and melt pockets are highlighted in red. The melt and grain preferred orientations obtained from these images are represented as rose diagrams in red and blue, respectively.

### *2.3 Melt network image analysis*

Melt pockets, which are 2-D sections through a 3-D melt network, were analyzed at the grain scale, where individual melt pockets are well resolved in the image (typically ~2000x magnification), and at the sample scale, over which larger patterns become apparent (typically ~200x magnification). To measure grain-scale MPO, individual pockets were traced from SEM-BSE, EDS, and band-contrast images such as those in Figure 3 and Figures 4a and 4b. These traced images were then converted to binary, black and white images for segmentation. Only pockets above a minimum size of 10 pixels (at pixel resolutions of 0.02 – 0.4 μm) were analyzed to avoid effects from poorly defined small melt pockets. We quantified the MPO and strength of alignment in a sample based on two factors, orientation ($\alpha_p$) and bulk aspect ratio ($b/a$), as described above.

To identify larger-scale melt patterns, we used EDS composition maps of calcium, an element present at sufficient concentration within the basaltic melt but not in the olivine used for these experiments. We segmented these maps to create binary images of individual melt pockets, which we analyzed using the ACF method over the entire sample imaged.

*2.4 Grain-shape preferred orientation and crystallographic preferred orientation analyses*

The shape preferred orientation was obtained from manual tracing of grains on SEM maps of the 2-D slices as well as from EBSD data. We characterize the shape preferred orientation of the grains in the same manner as the grain-scale MPO described above. Representative data are displayed in Figure 3.

EBSD data were collected at two scales, analogous to the melt network analyses. A low-resolution map (0.6-μm step size) covered large parts of the whole sample, and a high-resolution map (0.2-μm step size) focused on the intracrystalline deformation features, highlighted in Figures 4c-d. The EBSD data were analyzed using the MTEX toolbox () to characterize the 3-D orientation of the crystallographic axes. The crystallographic preferred orientation is defined by an ODF describing the direction of the three mutually perpendicular crystallographic axes in the olivine crystals in each sample. This ODF is represented graphically as a pole figure depicting multiples of uniform density (M.U.D.) in an equal-area, upper hemisphere projection, contoured by areas of high and low concentrations of each of the three crystallographic axes of olivine, as indicated in Figures 4e-f. We also collected the misorientations of the subgrains in the high-resolution EBSD maps, defined by the difference in internal pixel orientations from the mean orientation of an entire grain, which allowed us to examine internal deformation of grains.

*2.5 Calculation of seismic anisotropy*

To constrain the microstructural contributions of MPO and CPO to the generation of seismic anisotropy in olivine-melt aggregates, we followed the Gassman poroelastic differential effective medium method as applied in a Matlab model, GassDEM (Kim et al., 2019). This method uses the Voigt elastic tensor calculated from the CPO, then treats melt inclusions as an oriented fluid-filled crack.

We modeled melt pockets as penny-shaped ellipsoids, per Faul et al. (1994). The axes of these ellipsoids were defined as 1:*b/a*:1, where *b/a* is the shortest projection length of the melt pocket normalized by the longest projection length (equivalent to the *b*/*a* reported for all MPOs), and using the orientations of our MPOs such that the azimuth of an inclusion is the angle at which *b* is oriented with 0˚ = E and 90˚ = N. These orientations were rotated during input into the GassDEM interface, which takes 0˚ = N and 90˚ = W. We took the high-frequency elastic constants of the resultant tensor calculated with 2.5 wt% melt.

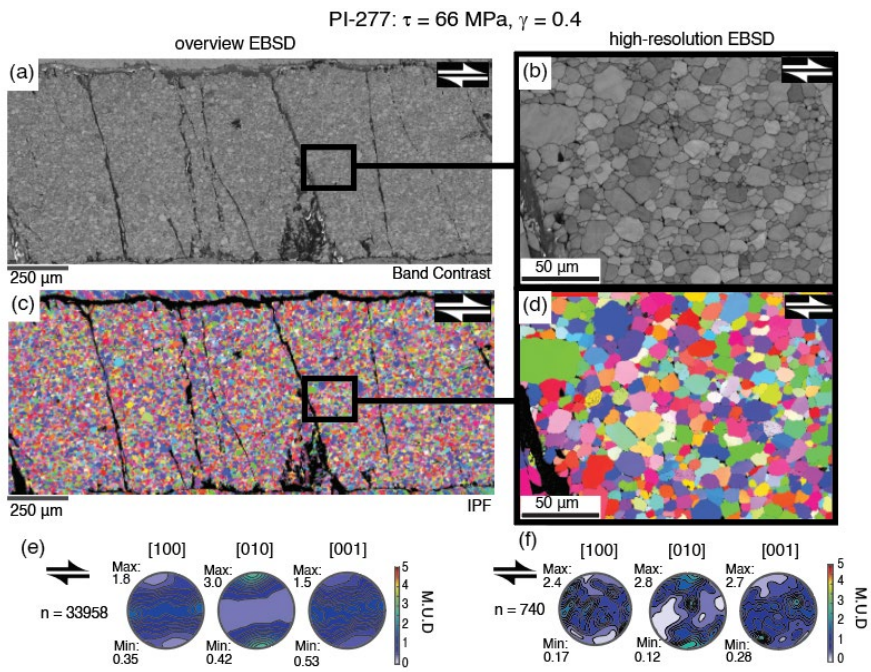


Figure 4: (a), (b) Band contrast images and (c), (d) orientation maps for sample PI-277. Pole figures are equal-area projections scaled as multiples of uniform distribution (M.U.D.). (e) Overview EBSD pole figures correspond to a larger number of crystals, while (f) high-resolution EBSD pole figures include a smaller number of crystals in greater detail, resulting in more pronounced point maxima.

## 3. **Results**

### *3.1 MPO - Melt preferred orientation*

### 3.1.1 Grain-scale melt alignment

Melt pockets reached a steady state-state orientation after a low degree of strain. The orientations of all individual melt pockets ("grain-scale" MPO), which were collected for all analyzed samples, are summarized in Figure 5. The melt preferred orientation in the starting material is very weak, with the *b*/*a* aspect ratio of 0.97 from all aggregated individual melt pockets indicating a nearly isotropic shape. The strength of the MPO increased at the onset of deformation and was fully established by $\gamma \approx 0.5$, with melt pockets oriented close to the loading direction at 135˚. The values of $\alpha_p$ of these deformed samples were essentially independent of strain (per linear fitting to establish a first-order relationship, $R^2 = 0.02$, p =0.77) such that the grain-scale MPO, once established, varied by only ±5º from parallel to the loading direction. There was a moderate dependence of orientation on stress ($R^2 = 0.64$, p = 0.06) within the studied range, with much of the variation due to the rotation of MPO in the highest stress test. The strongest alignment, a *b*/*a* ratio of 0.72, formed by a strain of $\gamma = 0.4$ (Figure 5b). Once established, *b/a* was insensitive to increasing strain ($R^2 = 0.008$, p = 0.95) and stress ($R^2 = 0.003$, p = 0.90).

Melt pocket sizes also converged to a common value at a low strain and did not evolve further with increasing strain, as demonstrated in Figure 5c. Melt pocket size in the starting material was $d_{equ} \approx 2$ µm, while melt pocket size shrank to $d_{equ} \approx 0.9$ µm by $\gamma = 0.4$ and converged to $d_{equ} \approx 0.5$ µm by $\gamma > 0.4$ in a manner that did not significantly depend on strain ($R^2 = 0.28$, p = 0.22) or stress ($R^2 = 0.42$, p = 0.11)

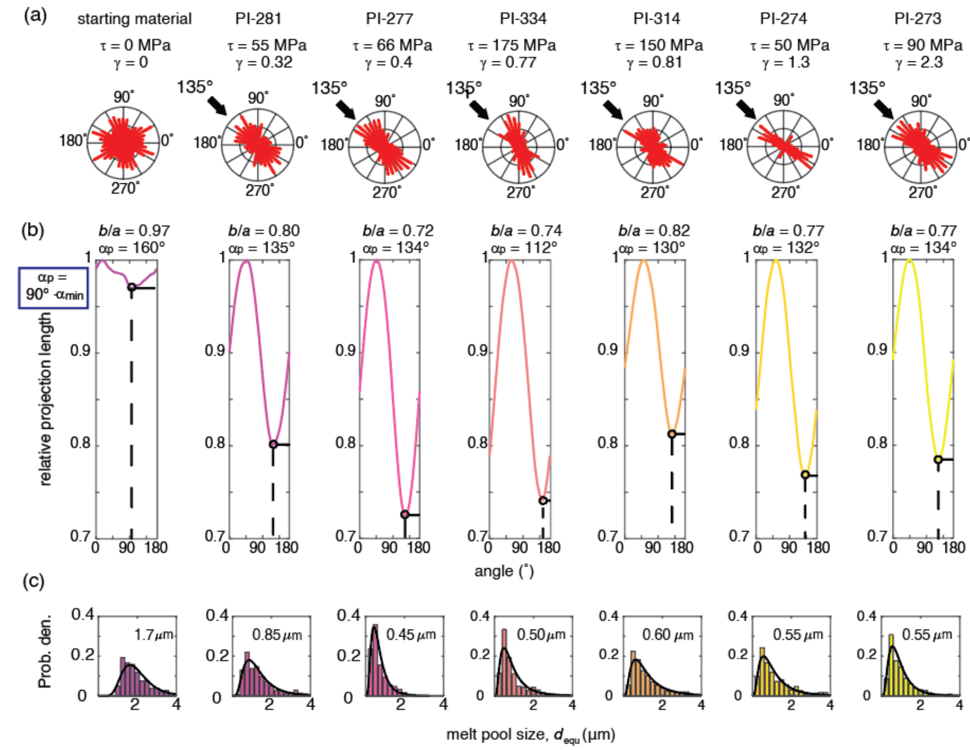


Figure 5: Evolution of MPO as a function of strain. (a) Rose diagrams from orientation of longest axes of each individual melt pocket. (b) Projection functions based on equation (1) with minima (shortest projection axis) and the corresponding preferred orientation labeled. (c) Melt pocket size histograms with log-normal fit overlain. The mode of the distribution is labeled.

### *3.1.2 Sample-scale melt alignment*

In addition to the grain-scale alignment, we observed larger patterns occuring over the spatial scale of the sample. The initial orientations and spatial distributions of all melt pockets at the "sample scale" were isotropic, as revealed by the ACF analyses of the binary images in Figure 7. At low strains, the spatial distribution of the melt remained isotropic, but the network of melt pockets developed a preferred orientation parallel to the loading direction at the sample scale, in agreement with the orientation of melt observed at the grain scale. In the samples deformed to the highest strain, melt began to segregate into relatively melt-rich and melt-poor regions, and a secondary orientation at long correlation length scales (i.e., the spatial distance over which a feature can be correlated with itself) began to form at ~155˚ (~20˚ to the loading direction). Short-correlation length scales (i.e., those close to the origin on the ACF plot) still retained an orientation sub-parallel to the loading direction.

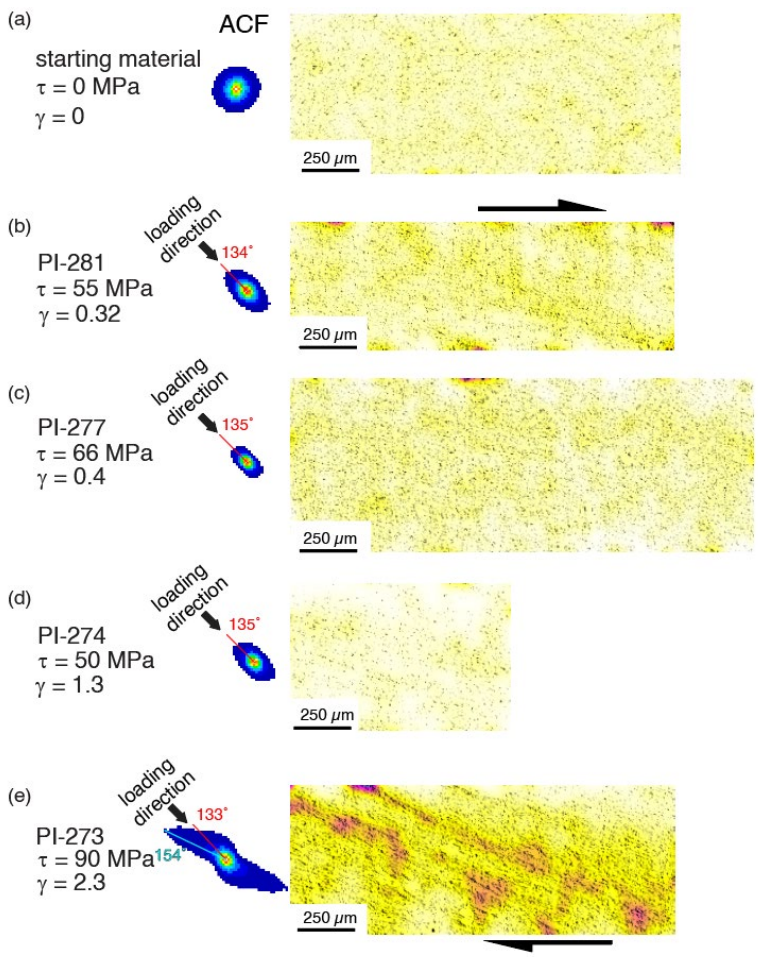


Figure 6: Sample-scale melt network analyzed by the autocorrelation function (ACF). Conditions of our (a) hot-pressed starting material and (b)-(e) four deformed samples with each corresponding ACF (central column) and binary melt map contoured from low melt density, in white, to high melt density, in purple (rightmost column). The distance from the center of an ACF represents the length scale over which a feature can be correlated (i.e., closer to center of an ACF = shorter-scale feature correlation, while further away from the center of the ACF = longer-scale feature correlation).

*3.2 Grain shape and crystallographic preferred orientation (SPO & CPO)*

*3.2.1 SPO - Shape preferred orientation*

Grains in the deformed samples established an SPO with increasing strain, but did not reach a steady state-state orientation over the range studied here. The SPO of all grains is reported in Figure 7. The long axes of grains were oriented at 10-20° from the shear plane of the sample at low strains and rotated to ~30° from the shear plane for $\gamma > 0.8$.

There was no clear dependence of the angle of preferred orientation, $\alpha_p$, on either strain (per linear fitting to establish a first-order relationship, $R^2 = 0.26$, $p = 0.30$) or stress ($R^2 = 0.26$, $p = 0.30$). However, the bulk grain shape aspect ratio, *b/a*, did depend on strain ($R^2 = 0.72$, $p = 0.016$), but not stress ($R^2 = 0.02$, $p = 0.76$). The aspect ratios remained close to isotropic (with a minimum of 0.88 at $\gamma = 0$ and a maximum of 0.94 at $\gamma = 0.3$) for all but the sample deformed to the highest strain. A stronger SPO, indicated by a *b*/*a* of 0.79, formed by $\gamma = 1.3$, as long axes of the deforming grains began to align.

Grain size generally decreased with increasing stress ($R^2 = 0.66$, $p = 0.026$) and was less sensitive to strain ($R^2 = 0.32$, $p = 0.16$). The distribution of grain sizes in the starting material (Figure 7c) peaked between $d_{equ} \approx 5$-$10$ µm after hot-pressing for 3 h. At $\gamma = 0.3$, grains exhibited a normal distribution curve with a peak at $d_{equ} \approx 9$ µm, while all samples deformed to higher strain had a log-normal distribution curve of grain sizes peaking at $d_{equ} \approx$ 2–4 µm.

Grain sizes, aspect ratios, and shape fabrics wavered were roughly independent of strain at low strains ($\gamma < 1.3$); at the highest strains examined here, both aspect ratios and grain sizes showed a decrease. The strength of the SPO was dependent on strain, but the orientation was not systematically dependent on stress or strain. SPO thus required higher strains to develop a steady state state orientation and was less sensitive to the early stages of deformation than MPO.

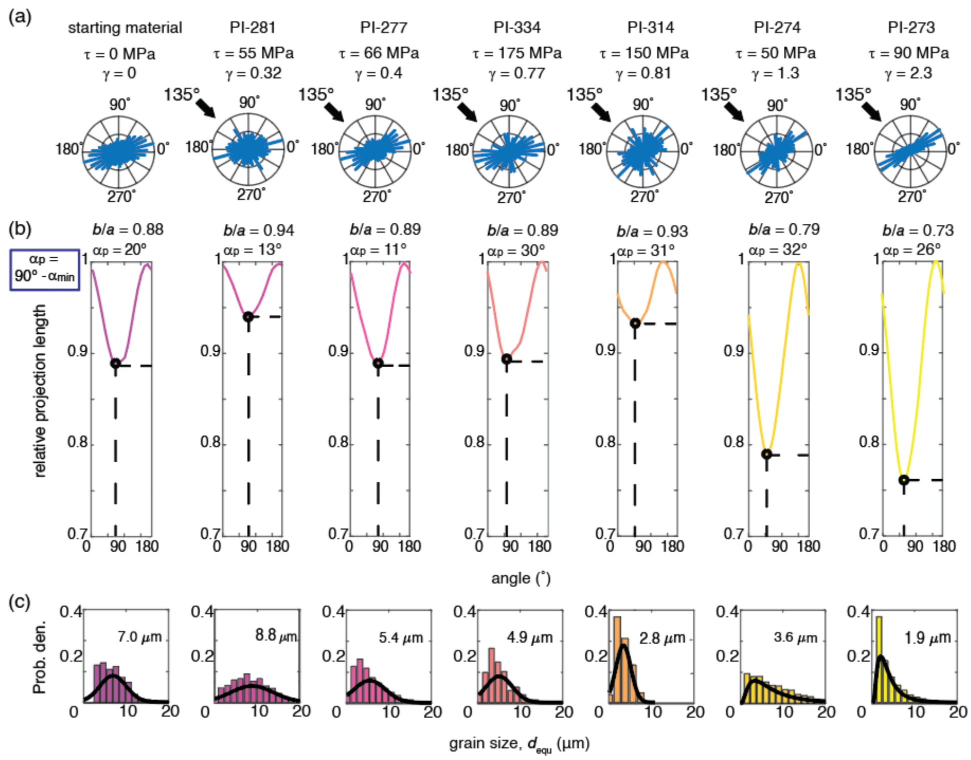


Figure 7: Grain SPO evolution as a function of strain. (a) Rose diagrams from orientation of longest axes of individual grains. (b) Projection functions based on equation (1) with minima (shortest projection axis) and the corresponding preferred orientation labeled. (c) Grain size distribution with normal or log-normal fit overlain. The mode of the distribution is labeled.

*3.2.2 CPO – Crystallographic preferred orientation*

The CPOs of deformed samples in Figure 8 evolved with increasing strain. The CPO was well-developed in the starting material with [010] axes aligned perpendicular to the shear plane of the sample and the [100] and [001] axes in weak girdles in the shear plane. As strain increased, alignment of the [010] axes increased in strength, while the [100] and [001] axes remained girdled. At low strains, the orientations rotated antithetically away from the shear plane, such that the [010] axes were 90-115° from the shear plane and the [100] and [001] axes girdled within 5° of the shear plane. At the highest strain reached in our experiments, $\gamma = 2.3$, the [100] axes began to cluster in the shear direction, while the [001] axes began to cluster in the center of the pole figure. A secondary maximum orientation of the [100] axes developed roughly perpendicular to the loading direction.

The density and misorientation of subgrains increased as strain increased, and the effect of increasing strain on intracrystalline structure is illustrated in Figure 9. As seen in Figure 9a, the subgrain density was low and misorientation angles were small (<10°) within subgrains in the starting material, while subgrains with relatively high misorientations (>10°) were present in nearly every grain in the sample deformed to $\gamma = 2.3$. Inverse pole figures of the misorientations in Figure 9 demonstrate that, with increasing strain, rotation around the [001] axis became increasingly common. The development of a subordinate maximum also suggests rotation around the [010] axis.

Similar to SPOs, CPOs did not change significantly in the early stages of deformation (Figure 8). The orientations of the crystallographic axes shifted only slightly, as the [010] planes first rotated antithetically to the shearing direction and then rotated into the shear plane. At strains of $\gamma = 1.3 – 2.3$, the [010] planes were rotated slightly synthetic to the imposed shear direction. The strength of the CPO generally increased as strain increased.

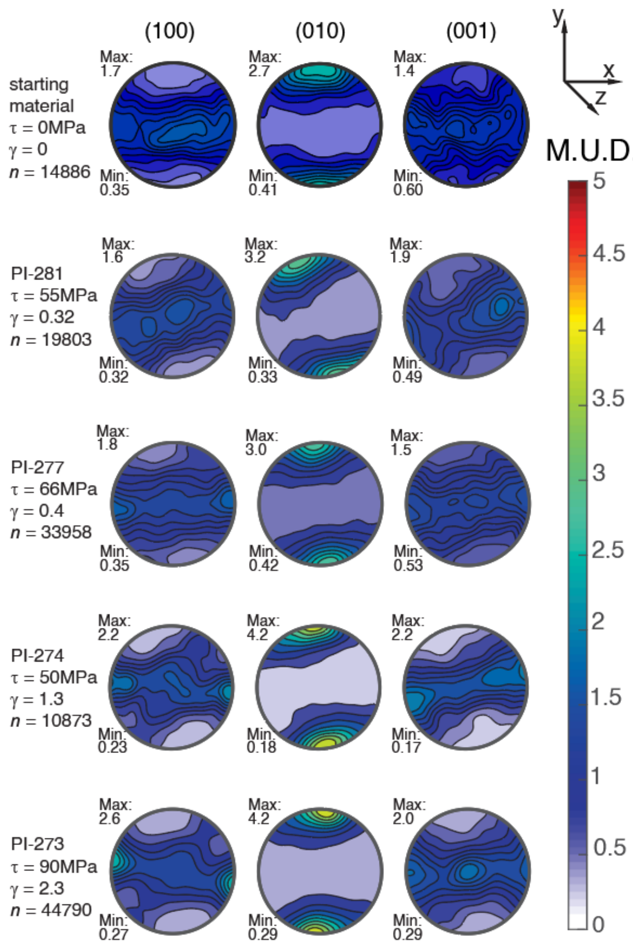


Figure 8: CPO evolution with increasing strain. Minima and maxima are reported as multiples of uniform distribution, M.U.D.; *n* is the number of grains surveyed in each map.

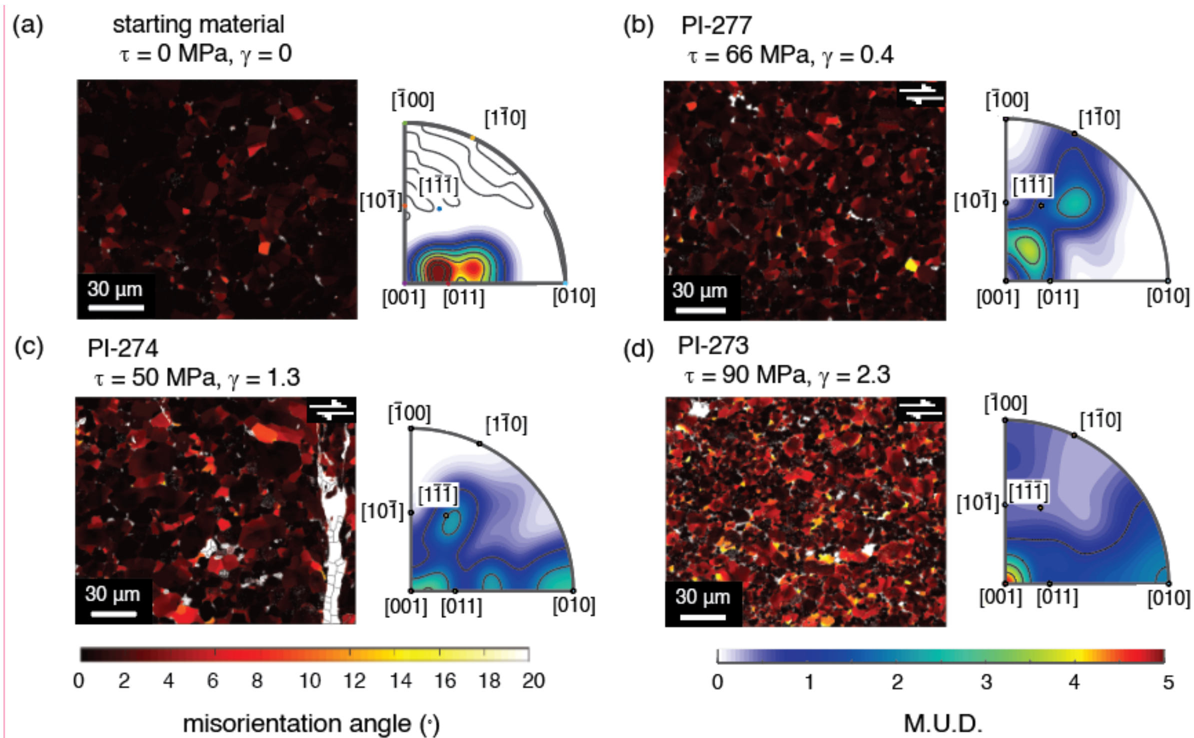


Figure 9: Misorientation maps and inverse pole figures of misorientation axes in the crystallographic reference frame from (a) the starting material, (b) a sample sheared to low strain, and (c)-(d) two samples deformed to high strain. All images are at the same scale.

*3,3 Calculation of seismic anisotropy*

We calculated seismic properties for each of our partially molten rocks, characterized in Figure 10 as the distribution of P wavespeed (Vp), the distribution of the normalized difference between the fast and slow S wavespeeds ($Vs_1$ and $Vs_2$), and the magnitude and polarization of $Vs_1$. We used three measures of seismic anisotropy, indicated as percentages within each tensor:

1) The normalized difference between the largest and the smallest values of P wavespeed (Vp), expressed in percent, calculated as $AV_p = 200\frac{(V_{Pmax}-V_{Pmin})}{(V_{Pmax}+V_{Pmin})}$;

2) the % difference in fast ($Vs_1$) and slow ($Vs_2$) S waves, calculated as the greatest difference between $Vs_1$ and $Vs_2$ within the tensor, and $AVs = 200\frac{(V_{S1}-V_{S2})}{(V_{S1}+V_{S2})}$ for every point in the tensor, with the maximum AVs reported;

3) the normalized difference between the largest and the smallest values of $Vs_1$, calculated as $AV_{S1} = 200\frac{\left(V_{S1}max - V_{S1}min\right)}{\left(V_{S1}max + V_{S1}min\right)}$.

The seismic anisotropy calculated in our deformed samples evolved over the studied strain intervals. Over a small increment of strain, the calculated values for the three indicators of the seismic anisotropy decreased. However, for samples deformed to $\gamma \gtrsim 1$, the calculated values of seismic anisotropy increased with increasing strain. This behavior parallels the development of MPOs and CPOs with increasing strain. At low strains, the CPO was weak, and the MPO was oriented antithetic to the shearing direction and parallel to the loading direction. The melt orientation was oblique to the orientation of the crystallographic axes, which were aligned in a girdle parallel to the shear plane. The anisotropy determined for our lower strain tests reflects a competition between MPO and CPO. As a result, inclusion of melt decreased the CPO-generated anisotropy with respect to a theoretical melt-free sample based on the same CPO. As strain increased, the strength and direction of the preferred orientation of the melt network did not change, but the CPO became stronger and the [100] axes became more aligned parallel to the shear plane. At higher strains, the seismic anisotropy of Vp, Vs, and $Vs_1$ all steadily increased. As the MPO remained at a steady state strength and orientation at these strains, this increase is due to the effect of CPO strengthening.

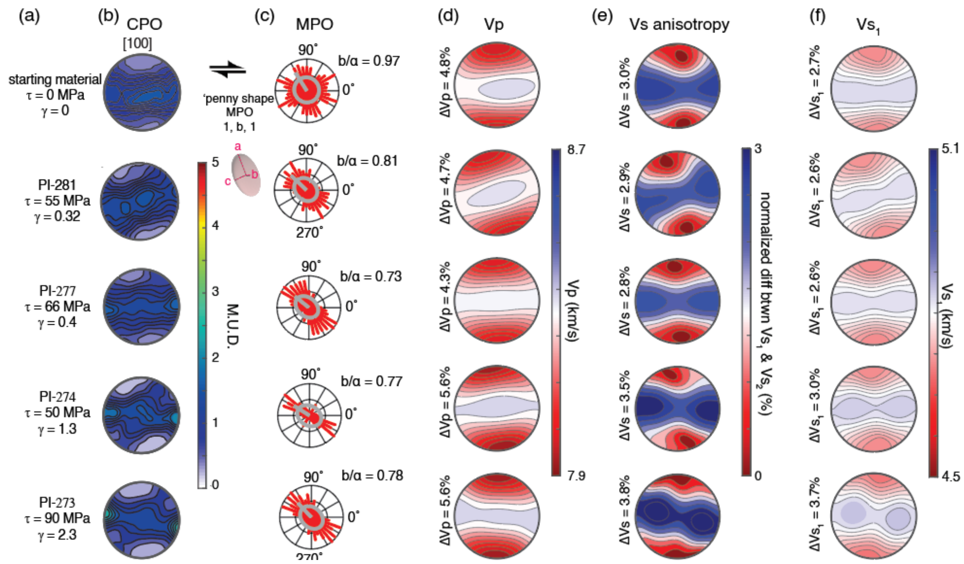


Figure 10. Calculated seismic anisotropy from our CPO and MPO data. (a) Individual experiment numbers and associated conditions, (b) a-axis orientation pole figures, and (c) MPO visualized in rose diagrams. The mean melt inclusion shape and orientation is represented as a gray ellipsoid superimposed on the rose diagrams. (d) Vp, (e) Vs anisotropy (normalized difference between orthogonally polarized $Vs_1$ and $Vs_2$), and (f) $Vs_1$ magnitude and polarization.

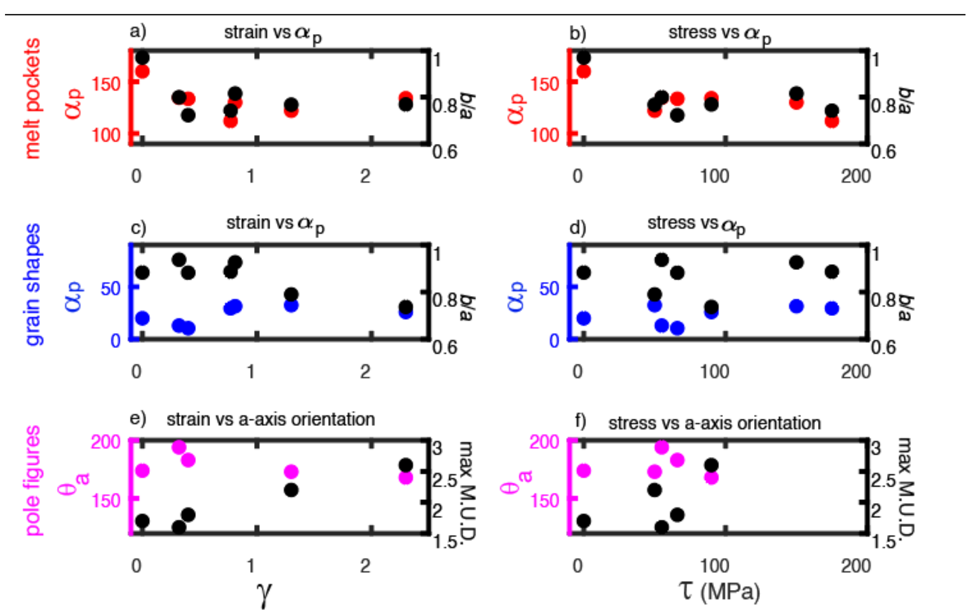


Figure 11. Summary of microstructural data. (a) Preferred orientation of melt pockets (from 0˚ = E) as a function of strain. (b) Preferred orientation of melt pockets as a

function of stress. (c) Preferred orientation of grain shapes as a function of strain. (d) Preferred orientation of grain shapes as a function of stress. In (a – d), Preferred orientation is reported as $\alpha_p$, and the strength of the preferred orientation is indicated by the aspect ratio *b*/*a* of the fabric. (e)Orientation of the girdle formed by olivine [100] axes ($\theta_a$) as a function of strain. (f) Orientation of the girdle formed by olivine [100] axes ($\theta_a$) as a function of stress. In (e-f) , the strength ofthe preferred orientation is reported as peak multiples of uniform distribution, such that a higher M.U.D. represents a higher concentration of axes aligned at this orientation. Note that CPO data are not available for the two tests carried out at the highest stresses.

## 4. Discussion

### *4.1 MPO formation on the grain scale and on the sample scale*

Our results demonstrate that MPO evolves much more quickly in response to shear deformation than either SPO or CPO of the solid grains, as summarized in Figure 11. A clear grain-scale MPO is evident in our lowest-strain sample deformed to $\gamma = 0.32$; however, a change in CPO and SPO is not apparent until $\gamma > 1$.

Previous examination of some of the samples used in this study with lower resolution optical images (tests PI-277, PI-281, PI-274, and PI-273, as reported in Zimmerman et al., 1999), led to the conclusion that the MPO is inclined at ~160˚ to the shear plane, antithetic to the shear direction (i.e., at ~25˚ to the loading direction). Likewise, analyses of low-resolution optical images of samples deformed in coaxial compression indicated that the MPO also formed at an angle of ~20˚ to the loading direction (Daines & Kohlstedt, 1997; Kohlstedt & Zimmerman, 1996; Zimmerman et al., 1999).

In contrast, our high-resolution SEM data demonstrate that the grain-scale melt pockets in these samples are aligned parallel to the loading direction. The MPO alignment in our tests is in agreement with observations on an analog material (Takei, 2005) and is consistent with the MPO needed to produce melt rich "bands" inclined 160 – 165˚ to the shear plane on the sample scale within the framework of two-phase flow theory with viscous anisotropy (Katz & Takei, 2013; Takei & Holtzman, 2009c, 2009b, 2009a; Takei & Katz, 2013; Taylor-West & Katz, 2015). Local variations in melt network orientation do exist, as seen in Figure 6; the orientation of larger melt pockets, perhaps as an aggregation of several smaller pockets, can produce local sub-maxima in orientation close to 155˚ in higher-strain samples in which incipient melt segregation is observed.

The scale of observation and the method of analysis (projection-based and autocorrelation-based methods vs. ellipse-fitting methods) may influence estimates of melt orientation. We propose that individual melt pockets at the grain scale align subparallel to the loading direction, while aggregated melt pockets on the sample scale form an en echelon pattern aligned at a lower angle with respect to the loading direction (Figure 6). This observation explains the discrepancy between experimentally obtained values of 155-165˚ for melt orientation and model assumptions of sub-parallel orientation with respect to applied maximum principal stress: both are correct, just at different observation scales.

Only our highest-strain sample developed incipient bands, similar to those in other experimentally sheared samples with a short compaction length that required strains of $\gamma \geq 1$ for bands to form (King et al., 2010; Kohlstedt & Holtzman, 2009). The emergence of these bands may then be the result of viscous anisotropy induced by grain-scale alignment of melt and decreasing compaction length as grains recrystallize to a smaller grain size, documented in Figure 7c. These observations again agree with predictions from the viscous anisotropy theory framework and the experiments designed to test this theory (Katz & Takei, 2013; Qi et al., 2015; Quintanilla-Terminel et al., 2019; Takei & Holtzman, 2009c)

*4.2 Stress state in general shear experiments*

We observed that, in response to an applied stress, individual melt pockets relatively quickly established a preferred orientation, which remained essentially constant with increasing strain. The preferred orientation for the individual melt pockets formed parallel to the loading direction, which is often assumed to coincide with the maximum principal stress ($\sigma_1$).

However, as general shear experiments include an element of thinning, it is possible that the $\sigma_1$ direction may not be aligned with the loading direction. Since stress state is not directly observed during our high-pressure experiments, we used strain as a proxy for understanding the contribution of thinning within the imposed stress field. This thinning provides insight into the relationship between the orientation of the effective $\sigma_1$ and that of the loading direction. If all the deformation were simple shear, $\sigma_1$ would remain oriented at 135˚, parallel to the applied load. As the contribution from pure shear increases, the maximum principal compressive stress would rotate away from the loading direction. We quantified the imposed finite strain geometry by measuring the sample thickness before and after deformation and calculating the kinematic vorticity number ($W_k$), which quantifies the degree of pure ($W_k \approx 0$) vs. simple ($W_k \approx 1$) shear during deformation (Fossen & Tikoff, 1993; Passchier, 1987). In our highest-stress test, $W_k$ = 0.92; for all other experiments, $W_k$ was >0.96 (see Table 1), indicating that the strain was close to simple shear. Throughout this paper, we have presented examples mostly from low-strain experiment PI-277 ($\gamma$ = 0.4, $W_k$ = 0.99) and high-strain experiment PI-273 ($\gamma$ = 2.3, $W_k$ = 0.98), both of which deformed primarily by simple shear. Additionally, the calculation of the $W_k$ assumes that thinning is consistent throughout deformation. Based on examination of samples annealed at high temperature and pressure but not deformed (e.g., starting material), most thinning occurs during the annealing and pressurization stage of experimental setup, and does not co-occur with shear deformation. The $W_k$ values therefore represent the lowest possible degree of simple shear, and the deformation experienced by the samples is probably closer to 100% simple shear (and thus, nearly no rotation of the $\sigma_1$ should occur). This result indicates that the $\sigma_1$ orientation is indeed close to the loading direction, at 135˚, consistent with the MPO.

Small-scale variations in MPO do occur, which may be related to the degree of pure vs simple shear in our experiments. The kinematic vorticity number, $W_k$ was lowest in our highest-stress test, indicating that this sample experienced a higher degree of pure shear than all others. In this high-stress test, the MPO rotated ~ 20˚ from the loading direction (synthetic to the sense of shear). A similar misalignment between loading direction and $\sigma_1$ was observed in qtz + feldspar samples deformed in general shear with a substantial thinning component; in these experiments, the stress orientation could be inferred via the development of Dauphiné twins in quartz (Pec & Al Nasser, 2021). Based on our observations, we propose that the grain-scale orientation of melt pockets can be used as an effective proxy for the orientation of the maximum principal stress.

*4.3 Grain SPO and CPO formation*

SPO and CPO evolve over higher strain intervals than MPO. Grains in the starting material had a SPO and a CPO that developed during hot pressing of the starting material. Individual olivine grains tend to be elongated along the [100] and [001] axes with the longest straight grain boundaries lying in the [010] plane (Miyazaki et al., 2013; Qi et al., 2018). Axial compression of these elongated crystals aligns the long axes of the SPO in a girdle perpendicular to the loading direction. This process results in a SPO-induced CPO, characterized by girdles in [100] and [001] axes oriented perpendicular to the loading direction and clusters in poles of [010] planes parallel to the loading direction, as seen in Figure 8.

The strength of CPO alignment increased visibly with increasing strain for $\gamma > 1$, consistent with numerical models (Boneh et al., 2015) and other experimental results (Boneh & Skemer, 2014; Hansen et al., 2014; Qi et al., 2018). Although the alignment strength increased, the evolution of grain size and shape fabric still did not depend systematically on strain or stress at low strains. The pole figure geometry also did not change significantly until a strain of $\gamma > 2$.

The CPO of the deformed samples is commonly observed in sheared aggregates of melt-bearing olivine. This CPO may develop if grains preferentially grow along the [001] direction and then align under the imposed kinematic boundary conditions; the relative fabric strength thus reflects competition between SPO-induced and dislocation-induced CPOs (Qi et al., 2018). Misorientation axes (Figure 9) also dominantly aligned with [001] with a subordinate maxima around [010] , indicating that (010)[100] is the dominant slip system in our rocks, given that the subgrain walls have a tilt character (Prior et al., 2002).

The CPOs of our higher strain samples are similar to that of an A-type fabric, indicative of the easy slip system (010)[100] accommodating deformation in the shear plane (Karato et al., 2008; Zhang & Karato, 1995). The CPO-generating mechanisms (SPO-induced CPO and dislocation-induced CPO) are likely competing at low strains; at higher strains, the more prominent cluster in [100] axes alignment in the shear direction, together with large intragranular misorientations, indicate that dislocation glide is dominant in formation of the CPO.

In the highest strain experiments, a secondary cluster in [100] axes orientations forms. This secondary maximum, though relatively common in A-type fabrics, is not well understood. Although Zhang et al. (2000) explained this secondary maximum as a signature of non-recrystallized grains in a matrix otherwise undergoing dynamic recrystallization, the grains with this orientation in our sample do not have substantially different misorientations from the bulk sample. They do, however, have a flatter and weaker SPO than all other grains in the sample.

*4.4 Contributions to seismic anisotropy*

The CPO alignment strengthens, but remains relatively static in orientation angle in samples sheared to strains of $\gamma \lesssim 2.5$. In contrast, the grain-scale melt network develops a distinct preferred orientation over a very small strain interval, and the strength and angle of this orientation persists with increasing strain. The strength of the melt alignment saturates at low strains and does not increase with increasing strain or stress, as can be observed in Figure 5.

It follows that at early strain increments of deformation within the Earth, changes in the orientation of the melt network will cause changes in seismic anisotropy. The CPO, which evolves more slowly than MPO, will not contribute significantly to the seismic anisotropy until larger strains are reached. Previous studies of seismic anisotropy caused by an aligned melt network in a rock with an isotropic CPO determined the strength of anisotropy caused purely by melt orientation (Lee et al., 2017). In a series of calculations with the GassDEM model that covered a range of hypothetical MPOs and crystalline fabrics, we found that the interplay of MPO and CPO is crucial to modeling actual seismic anisotropy. As an example, we present theoretical seismic properties for deformed sample PI-277 in Figure 12.

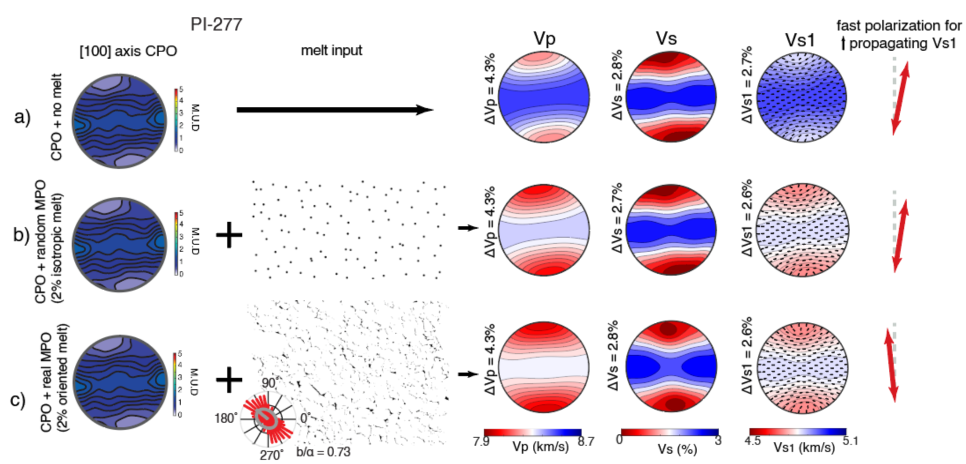


Figure 12: Seismic properties for deformed sample PI-277 using (a) the CPO alone, (b) the CPO and isotropic melt (idealized as circular melt inclusions), and (c) the CPO and aligned melt to create the elastic tensors. P wavespeeds (Vp), Vs anisotropy, and fast S-wave speeds ($Vs_1$) are shown in each case, along with the fast polarization direction for the $Vs_1$ wave traveling vertically through the sample.

The addition of isotropic (equiaxial) melt pockets reduces seismic velocities and CPO-induced anisotropies but does not interact with the CPO-generated anisotropy (as in Figure 12b), and so its effect is less pronounced than that of oriented melt (Figure 12c). The presence of aligned melt alone reduced seismic wavespeeds and influenced seismic anisotropies (Figure 12c), but the relative alignment of the MPO and CPO determined the extent and magnitude of this change. The [100] axes of olivine and the angle of the MPO each indicate a likely fast direction, so seismic anisotropy is highest if the [100] axes and the MPO are in a similar orientation. Seismic velocities and anisotropies both decrease at the onset of deformation caused by a change in stress; when the stress changes and a MPO forms or reforms, the new fast direction induced by the MPO competes with the steady state state [100] alignment. However, calculated seismic anisotropy increases above $\gamma \approx 0.8$, as the CPO strengthens and the MPO remains unchanged (Figures 10 and 11). The magnitude of this effect depends on melt fraction as well, as the effect of co-aligned MPO and CPO increases with increasing melt fraction. Anisotropy in P wavespeed (Vp), relative travel times of Vs, and $V_{S1}$ all followed the trend described here, with $V_{S1}$ anisotropy being particularly sensitive to the effect of melt fraction.

The polarization of a vertically propagating S-wave (not necessarily a vertically *polarized* S-wave; here, we use $V_{S1}$ rather than $V_{SH}$ or $V_{SV}$) is also particularly sensitive to the orientation of melt: the addition of isotropic melt does not change this polarization direction, but the orientation of the same degree of melt can rotate the fast direction by over 15°. Studies of CPO within the Earth, which invoke vertically propagating waves to explain seismic anisotropy thus may significantly mispredict the orientation of olivine axes.

*4.5 Application to natural settings*

Measurements of seismic anisotropy in the Earth's lithosphere are traditionally understood to result from CPOs, such that seismologists can use anisotropy measurements to infer the direction of flow in the mantle (Long & Becker, 2010). However, this approach does not sufficiently account for the presence and orientation of melt (Holtzman and Kendall, 2010; Mainprice, 1997).

Our results demonstrate that CPOs and MPOs evolve over distinct characteristic timescales, complicating the interpretation of observed seismic anisotropy in terms of oriented mantle flow. Natural strain rates are much slower than laboratory experiments, and the process of overprinting extant CPOs during deformation likely involves a long transient interval (Boneh et al., 2015). MPOs, however, require very small strain intervals to change, so the MPOs forming due to changing stress will compete with established, steady state-state CPOs.

As such, abrupt changes to local stress field, such as those caused for example by an earthquake or volcanic eruption, would only be visible in short-term perturbations to seismic anisotropy as a result of readjustment of the orientation of the melt network. The almost instantaneous development of MPO in response to an applied differential stress also means that MPO is a more reliable indicator of instantaneous changes in stress than the CPO. This behavior of melt may be useful for observing results of stress changes within the Earth or for understanding melt distribution in rapidly evolving planetary settings dominated by orbital tidal stresses.

We can look to seismic studies of the Earth's crust for confirmation. Some crustal seismic anisotropy is thought to result from the orientation of magmatic intrusions (Frothingham et al., 2023; Hammond, 2014) and fluid-filled microcracks (Crampin, 1987; Crampin & Zatsepin, 1997; Elkibbi et al., 2005) that form parallel to the local maximum compressive stress (Gerst & Savage, 2004; Johnson, 2015). Within geophysically observable timescales, microscale crystallographic orientation is considered to be relatively static. Volcanically active crustal regions undergo short-term changes to magnitude and orientation of shear wave anisotropy during episodes of melt infiltration (Araragi et al., 2015; Illsley-Kemp et al., 2018; Johnson et al., 2015), allowing researchers to track the local stress and deformation fields using anisotropy measurements as a tracer for movement of melt.

Treating a small amount of melt as an oriented inclusion with distinct poroelastic properties is a tested approach to interpreting seismic anisotropy in rapidly deforming regions. Our results indicate possible similarities in the seismic signatures of the melt-intruded crust and partially molten mantle, suggesting that tomographic techniques used to infer near-surface stress and deformation could be applied to signals from deeper in the Earth. Studies of fast-deforming zones in Eastern Africa have previously inferred that melt alignment contributes noticeably to seismic anisotropy in the shallow upper mantle (Bastow et al., 2010; Chambers et al., 2021; Hammond, 2014; Kendall et al., 2005), and this framework may also be applicable to evolving seismic anisotropy in subduction zones and mid-ocean ridges.

## 5. Conclusions

As a partially molten olivine-basalt aggregate deforms,

- Grain-scale melt alignment forms parallel to the loading direction at relatively low strain ($0 < \gamma < 0.3$) and persists to the highest strains studied here. Strain does not affect the orientation or strength of this grain-scale melt alignment above this interval.
- A *grain-scale* melt preferred orientation forms parallel to the inferred local maximum compressive principal stress ($\sigma_1$), which may rotate away from the applied $\sigma_1$ with increasing shear stress or thinning.
- A distinct *sample-scale* melt preferred orientation forms at 155° (20˚ oblique to the loading direction) at higher strain due to en echelon arrangement of grain-scale melt pockets and incipient melt segregation.
- The CPO that developed during hot pressing does not change significantly in orientation during subsequent deformation. However, the strength of the CPO increases steadily with increasing strain.
- The relatively weak SPO produced during hot-pressing randomized at low to intermediate strains $0.3 < \gamma < 1.3$, and grains develop a moderately strong SPO oriented at ~30˚ to the shear plane at high strains ($\gamma > 1.3$).
- A MPO is established more quickly in response to changes in the stress field than is a CPO or SPO.
- Once established grain-scale MPO does not change with increasing strain, but the sample-scale melt network coalesces into bands with a distinct orientation. At higher strains, the dislocation-induced CPO strengthens and contributes more to seismic anisotropy than does the MPO.
- Immediately after a change in stress field, seismic anisotropy will be more affected by changes to the MPO than by changes to the CPO. At small strains or over short observable timescales, the MPO thus provides insight into the orientation of the stress field in quickly deforming regions of the Earth's upper mantle in ways that CPO-induced anisotropy cannot.

Acknowledgments:

We thank Benjamin Holtzman for commentary and discussion in earlier stages of this project, Rüdiger Kilian for support with MTEX, Fabrice Barou for providing EBSD maps, and David

Mainprice for connecting us with Eunyoung Kim who provided support with GassDEM. This work benefited strongly from the suggestions of Richard Katz and an anonymous reviewer. We thank Hamed O'Ghaffari for developing COMSOL models to study the stress orientations in the experiments. This work was supported by NSF-EAR 1753482 and NASA-SSW-80NSSC20K0465, with laboratory technician support funded by NSF-EAR 2054414. C.S. also received support from the MIT MathWorks Science Fellowship.

Data availability:

Melt maps, EBSD, and analyzed bulk MPO/SPO data are available at 10.5281/zenodo.7647271 (Seltzer, 2023).

References:

Almqvist, B. S. G., & Mainprice, D. (2017). Seismic properties and anisotropy of the continental crust: Predictions based on mineral texture and rock microstructure. *Reviews of Geophysics*, *55*(2), 367–433. https://doi.org/10.1002/2016RG000552

Araragi, K. R., Savage, M. K., Ohminato, T., & Aoki, Y. (2015). Seismic anisotropy of the upper crust around Mount Fuji, Japan. *Journal of Geophysical Research: Solid Earth*, *120*(4), 2739–2751. https://doi.org/10.1002/2014JB011554

Bastow, I. D., Pilidou, S., Kendall, J.-M., & Stuart, G. W. (2010). Melt-induced seismic anisotropy and magma assisted rifting in Ethiopia: Evidence from surface waves. *Geochemistry, Geophysics, Geosystems*, *11*(6). https://doi.org/10.1029/2010GC003036

Blackman, D. K., & Kendall, J.-M. (1997). Sensitivity of teleseismic body waves to mineral texture and melt in the mantle beneath a mid–ocean ridge. *Philosophical Transactions of the Royal Society of London. Series A: Mathematical, Physical and Engineering Sciences*, *355*(1723), 217–231.

Boneh, Y., Morales, L. F. G., Kaminski, E., & Skemer, P. (2015). Modeling olivine CPO evolution with complex deformation histories: Implications for the interpretation of seismic anisotropy in the mantle. *Geochemistry, Geophysics, Geosystems*, *16*(10), 3436–3455. https://doi.org/10.1002/2015GC005964

Boneh, Y., & Skemer, P. (2014). The effect of deformation history on the evolution of olivine CPO. *Earth and Planetary Science Letters*, *406*, 213–222. https://doi.org/10.1016/j.epsl.2014.09.018

Chambers, E. L., Harmon, N., Rychert, C. A., & Keir, D. (2021). Variations in melt emplacement beneath the northern East African Rift from radial anisotropy. *Earth and Planetary Science Letters*, *573*, 117150. https://doi.org/10.1016/j.epsl.2021.117150

Cooper, R. F., & Kohlstedt, D. L. (1984). Solution-precipitation enhanced diffusional creep of partially molten olivine-basalt aggregates during hot-pressing. *Tectonophysics*, *107*(3), 207–233. https://doi.org/10.1016/0040-1951(84)90252-X

Crampin, S. (1987). Geological and industrial implications of extensive-dilatancy anisotropy. *Nature*, *328*(6130), Article 6130. https://doi.org/10.1038/328491a0

Crampin, S., & Zatsepin, S. V. (1997). Modelling the compliance of crustal rock—II. Response to temporal changes before earthquakes. *Geophysical Journal International*, *129*(3), 495–506. https://doi.org/10.1111/j.1365-246X.1997.tb04489.x

Daines, M. J., & Kohlstedt, D. L. (1997). Influence of deformation on melt topology in peridotites. *Journal of Geophysical Research: Solid Earth*, *102*(B5), 10257–10271. https://doi.org/10.1029/97JB00393

Elkibbi, M., Yang, M., & Rial, J. A. (2005). Crack-induced anisotropy models in The Geysers geothermal field. *Geophysical Journal International*, *162*(3), 1036–1048. https://doi.org/10.1111/j.1365-246X.2005.02697.x

Faul, U. H., Toomey, D. R., & Waff, H. S. (1994). Intergranular basaltic melt is distributed in thin, elogated inclusions. *Geophysical Research Letters*, *21*(1), 29–32. https://doi.org/10.1029/93GL03051

Fossen, H., & Tikoff, B. (1993). The deformation matrix for simultaneous simple shearing, pure shearing and volume change, and its application to transpression-transtension tectonics. *Journal of Structural Geology*, *15*(3), 413–422. https://doi.org/10.1016/0191-8141(93)90137-Y

Frothingham, M. G., Mahan, K. H., Schulte-Pelkum, V., Goncalves, P., & Zucali, M. (2023). Confronting Solid-State Shear Bias: Magmatic Fabric Contribution to Crustal Seismic Anisotropy. *Geophysical Research Letters*, *50*(6), e2022GL102399. https://doi.org/10.1029/2022GL102399

Gerst, A., & Savage, M. K. (2004). Seismic Anisotropy Beneath Ruapehu Volcano: A Possible Eruption Forecasting Tool. *Science*, *306*(5701), 1543–1547. https://doi.org/10.1126/science.1103445

Hammond, J. O. S. (2014). Constraining melt geometries beneath the Afar Depression, Ethiopia from teleseismic receiver functions: The anisotropic H-κ stacking technique. *Geochemistry, Geophysics, Geosystems*, *15*(4), 1316–1332. https://doi.org/10.1002/2013GC005186

Hansen, L. N., Faccenda, M., & Warren, J. M. (2021). A review of mechanisms generating seismic anisotropy in the upper mantle. *Physics of the Earth and Planetary Interiors*, *313*, 106662. https://doi.org/10.1016/j.pepi.2021.106662

Hansen, L. N., Zhao, Y.-H., Zimmerman, M. E., & Kohlstedt, D. L. (2014). Protracted fabric evolution in olivine: Implications for the relationship among strain, crystallographic fabric, and seismic anisotropy. *Earth and Planetary Science Letters*, *387*, 157–168. https://doi.org/10.1016/j.epsl.2013.11.009

Heilbronner, R., & Barrett, S. (2014). *Image Analysis in Earth Sciences: Microstructures and Textures of Earth Materials*. Springer-Verlag. https://doi.org/10.1007/978-3-642-10343-8

Hier-Majumder, S. (2011). Development of anisotropic mobility during two-phase flow. *Geophysical Journal International*, *186*(1), 59–68. https://doi.org/10.1111/j.1365-246X.2011.05024.x

Holtzman, B. K., Groebner, N. J., Zimmerman, M. E., Ginsberg, S. B., & Kohlstedt, D. L. (2003). Stress-driven melt segregation in partially molten rocks. *Geochemistry, Geophysics, Geosystems*, *4*(5). https://doi.org/10.1029/2001GC000258

Holtzman, B. K., & Kendall, J.-M. (2010). Organized melt, seismic anisotropy, and plate boundary lubrication. *Geochemistry, Geophysics, Geosystems*, *11*(12). https://doi.org/10.1029/2010GC003296

Illsley-Kemp, F., Greenfield, T., & Keir, D. (2018). Seismic Anisotropy Reveals a Dynamic Link Between Adjacent Magmatic Segments Prior to Dyke Intrusion. *Journal of Geophysical Research: Solid Earth*, *123*(11), 9800–9816. https://doi.org/10.1029/2018JB016420

Johnson, J. H. (2015). Seismic Anisotropy in Volcanic Regions. In M. Beer, I. A. Kougioumtzoglou, E. Patelli, & S.-K. Au (Eds.), *Encyclopedia of Earthquake Engineering* (pp. 2692–2706). Springer. https://doi.org/10.1007/978-3-642-35344-4_44

Johnson, J. H., Swanson, D. A., Roman, D. C., Poland, M. P., & Thelen, W. A. (2015). Crustal Stress and Structure at Kīlauea Volcano Inferred from Seismic Anisotropy. In *Hawaiian Volcanoes* (pp. 251–268). American Geophysical Union (AGU). https://doi.org/10.1002/9781118872079.ch12

Karato, S., Jung, H., Katayama, I., & Skemer, P. (2008). Geodynamic Significance of Seismic Anisotropy of the Upper Mantle: New Insights from Laboratory Studies. *Annual Review of Earth and Planetary Sciences*, *36*(1), 59–95. https://doi.org/10.1146/annurev.earth.36.031207.124120

Katz, R. F., & Takei, Y. (2013). Consequences of viscous anisotropy in a deforming, two-phase aggregate. Part 2. Numerical solutions of the full equations. *Journal of Fluid Mechanics*, *734*, 456–485. https://doi.org/10.1017/jfm.2013.483

Kendall, J.-M., Stuart, G. W., Ebinger, C. J., Bastow, I. D., & Keir, D. (2005). Magma-assisted rifting in Ethiopia. *Nature*, *433*(7022), Article 7022. https://doi.org/10.1038/nature03161

Kim, E., Kim, Y., & Mainprice, D. (2019). GassDem: A MATLAB program for modeling the anisotropic seismic properties of porous medium using differential effective medium theory and Gassmann's poroelastic relationship. *Computers & Geosciences*, *126*, 131–141. https://doi.org/10.1016/j.cageo.2019.02.008

King, D. S. H., Zimmerman, M. E., & Kohlstedt, D. L. (2010). Stress-driven Melt Segregation in Partially Molten Olivine-rich Rocks Deformed in Torsion. *Journal of Petrology*, *51*(1–2), 21–42. https://doi.org/10.1093/petrology/egp062

Kohlstedt, D. L., & Holtzman, B. K. (2009). Shearing Melt Out of the Earth: An Experimentalist's Perspective on the Influence of Deformation on Melt Extraction. *Annual Review of Earth and Planetary Sciences*, *37*(1), 561–593. https://doi.org/10.1146/annurev.earth.031208.100104

Kohlstedt, D. L., & Zimmerman, M. E. (1996). Rheology of Partially Molten Mantle Rocks. *Annual Review of Earth and Planetary Sciences*, *24*(1), 41–62. https://doi.org/10.1146/annurev.earth.24.1.41

Lee, A. L., Walker, A. M., Lloyd, G. E., & Torvela, T. (2017). Modeling the impact of melt on seismic properties during mountain building. *Geochemistry, Geophysics, Geosystems*, *18*(3), 1090–1110. https://doi.org/10.1002/2016GC006705

Long, M. D., & Becker, T. W. (2010). Mantle dynamics and seismic anisotropy. *Earth and Planetary Science Letters*, *297*(3), 341–354. https://doi.org/10.1016/j.epsl.2010.06.036

Lyakhovsky, V., Shalev, E., Kurzon, I., Zhu, W., Montesi, L., & Shapiro, N. M. (2021). Effective seismic wave velocities and attenuation in partially molten rocks. *Earth and Planetary Science Letters*, *572*, 117117. https://doi.org/10.1016/j.epsl.2021.117117

Miyazaki, T., Sueyoshi, K., & Hiraga, T. (2013). Olivine crystals align during diffusion creep of Earth's upper mantle. *Nature*, *502*(7471), Article 7471. https://doi.org/10.1038/nature12570

Passchier, C. W. (1987). Stable positions of rigid objects in non-coaxial flow—A study in vorticity analysis. *Journal of Structural Geology*, *9*(5), 679–690. https://doi.org/10.1016/0191-8141(87)90152-0

Paterson, M. S. (1990). Rock Deformation Experimentation. In *The Brittle-Ductile Transition in Rocks* (pp. 187–194). American Geophysical Union (AGU). https://doi.org/10.1029/GM056p0187

Pec, M., & Al Nasser, S. (2021). Formation of Nanocrystalline and Amorphous Materials Causes Parallel Brittle-Viscous Flow of Crustal Rocks: Experiments on Quartz-Feldspar Aggregates. *Journal of Geophysical Research: Solid Earth*, *126*(5), e2020JB021262. https://doi.org/10.1029/2020JB021262

Prior, D. J., Wheeler, J., Peruzzo, L., Spiess, R., & Storey, C. (2002). Some garnet microstructures: An illustration of the potential of orientation maps and misorientation analysis in microstructural studies. *Journal of Structural Geology*, *24*(6), 999–1011. https://doi.org/10.1016/S0191-8141(01)00087-6

Qi, C., Hansen, L. N., Wallis, D., Holtzman, B. K., & Kohlstedt, D. L. (2018). Crystallographic Preferred Orientation of Olivine in Sheared Partially Molten Rocks: The Source of the “a-c Switch.” *Geochemistry, Geophysics, Geosystems*, *19*(2), 316–336. https://doi.org/10.1002/2017GC007309

Qi, C., Kohlstedt, D. L., Katz, R. F., & Takei, Y. (2015). Experimental test of the viscous anisotropy hypothesis for partially molten rocks. *Proceedings of the National Academy of Sciences*, *112*(41), 12616–12620. https://doi.org/10.1073/pnas.1513790112

Quintanilla-Terminel, A., Dillman, A. M., Pec, M., Diedrich, G., & Kohlstedt, D. L. (2019). Radial Melt Segregation During Extrusion of Partially Molten Rocks. *Geochemistry, Geophysics, Geosystems*, *20*(6), 2985–2996. https://doi.org/10.1029/2018GC008168

Savage, M. K. (1999). Seismic anisotropy and mantle deformation: What have we learned from shear wave splitting? *Reviews of Geophysics*, *37*(1), 65–106. https://doi.org/10.1029/98RG02075

Seltzer, C. (2023). *Supplementary information for  Melt network reorientation and crystallographic preferred orientation development in sheared partially molten rocks*. https://doi.org/10.5281/zenodo.7647271

Takei, Y. (2005). Deformation-induced grain boundary wetting and its effects on the acoustic and rheological properties of partially molten rock analogue. *Journal of Geophysical Research: Solid Earth*, *110*(B12). https://doi.org/10.1029/2005JB003801

Takei, Y., & Holtzman, B. K. (2009a). Viscous constitutive relations of solid-liquid composites in terms of grain boundary contiguity: 1. Grain boundary diffusion control model. *Journal of Geophysical Research: Solid Earth*, *114*(B6). https://doi.org/10.1029/2008JB005850

Takei, Y., & Holtzman, B. K. (2009b). Viscous constitutive relations of solid-liquid composites in terms of grain boundary contiguity: 2. Compositional model for small melt fractions. *Journal of Geophysical Research: Solid Earth*, *114*(B6). https://doi.org/10.1029/2008JB005851

Takei, Y., & Holtzman, B. K. (2009c). Viscous constitutive relations of solid-liquid composites in terms of grain boundary contiguity: 3. Causes and consequences of viscous anisotropy. *Journal of Geophysical Research: Solid Earth*, *114*(B6). https://doi.org/10.1029/2008JB005852

Takei, Y., & Katz, R. F. (2013). Consequences of viscous anisotropy in a deforming, two-phase aggregate. Part 1. Governing equations and linearized analysis. *Journal of Fluid Mechanics*, *734*, 424–455. https://doi.org/10.1017/jfm.2013.482

Taylor-West, J., & Katz, R. F. (2015). Melt-preferred orientation, anisotropic permeability and melt-band formation in a deforming, partially molten aggregate. *Geophysical Journal International*, *203*(2), 1253–1262. https://doi.org/10.1093/gji/ggv372

Zhang, S., & Karato, S. (1995). Lattice preferred orientation of olivine aggregates deformed in simple shear. *Nature*, *375*(6534), 774–777. https://doi.org/10.1038/375774a0

Zhang, S., Karato, S., Fitz Gerald, J., Faul, U. H., & Zhou, Y. (2000). Simple shear deformation of olivine aggregates. *Tectonophysics*, *316*(1–2), 133–152. https://doi.org/10.1016/S0040-1951(99)00229-2

Zimmerman, M. E., Zhang, S., Kohlstedt, D. L., & Karato, S. (1999). Melt distribution in mantle rocks deformed in shear. *Geophysical Research Letters*, *26*(10), 1505–1508. https://doi.org/10.1029/1999GL900259